Near-infrared transparent conductive electrodes based on composite GaAs-metal deep sub-wavelength high contrast grating: supplemental document

Natan Monvoisin[1], Weronika Głowadzka[2], Franck Carcenac[1], Stéphane Calvez[1], Olivier Gauthier-Lafaye[1], Antoine Monmayrant[1], Marcin Gębski[2], Tomasz Czyszanowski[2], and Guilhem Almuneau[1,*]

[1]LAAS-CNRS, Université de Toulouse, CNRS, INSA, 31400 Toulouse, France
[2]Technical University of Łódź, Laboratory of Photonics Institute of Physics, 90-924 Łódź, Poland

E-mail: *almuneau@laas.fr

30 October 2024

Abstract. This supplement file presents complementary data that might be relevant for the reader, reporting comprehensive details about the structure and the fabrication steps of the studied samples and their optical and electrical characterizations methods and results.

1. Design and fabrication of transparent MetalMHCG structures

The description of the six MetalMHCG designed structures are summarized in table S1. These geometrical parameters are used for the RCWA calculation and the reflectivity mappings in figure 2 of the main document.

2. Fabrication process flow

Two distinct, albeit fairly similar, fabrication processes have been developed to fabricate the B-TE and T-TM MetalMHCG structures. The schematic description of the B-TE and T-TM configurations process are presented in Figures S1a and S1b respectively. The alignment of the GaAs and metal gratings is ensured by the self-aligned nature of these two processes. The process for the B-TE configuration begins with the chemical cleaning and de-oxidation of the GaAs wafer. Subsequently, a 40-by-40 μm^2 grating pattern is defined by electron beam lithography (EBL) on the wafer using a positive (CSAR62) resist. This high-resolution resist is selected for its excellent plasma etching resistance that is crucial for this process flow as, indeed, a GaAs dry-etching step precedes the metal deposition and lift-off processes. To ensure proper adhesion

Table S1: MetalMHCG parameters of the targeted structures in fabrication. The dimensions are extracted from calculations in Figure 2.

	MetalMHCG parameters					
Structure name	Λ (nm)	F	H(nm)	H_{Au} (nm)	H_{Ti} (nm)	Theoretical transmission ($\lambda = 940$ nm)
B-TE-Au-1	170	0.6	80	50	—	96% (TE)
B-TE-Au-2	210	0.5	85	50	—	96% (TE)
B-TE-TiAu-1	180	0.6	85	50	5	92% (TE)
B-TE-TiAu-2	220	0.5	90	50	5	92% (TE)
T-TM-Au	150	0.5	40	50	—	95% (TM)
T-TM-TiAu	100	0.5	80	50	5	83% (TM)

to the GaAs surface, the use of HMDS promoter is necessary. The use of 9% diluted solution of CSAR62 results in a suitable resist thickness of approximately 180 nm. After etching, the resist thickness reduces to around 140 nm, remaining compatible with the subsequent lift-off process involving the electron beam evaporation of a 50-55 nm-thick metal with deep sub-micrometric lines width. The semiconductor grating is etched using inductively coupled plasma reactive ion etching (ICP-RIE) with a Cl_2/N_2 gas mixture, achieving an etch rate of $\sim$ 4.8nm/s. Following the etching step, Au (50 nm) or TiAu (5/50 nm) is deposited using electron beam evaporation. Chemical oxide removal is applied before these main steps. The final lift-off step involves an 8-hour immersion in an 80°C DMSO solvent, followed, if necessary, by an ultrasonic bath and spraying with acetone. The process flow for the T-TM configurations begins with a similar EBL pattern-writing step, utilizing PMMA positive resist diluted at 38 g/L in anisole. This choice aims to achieve good adhesion on GaAs while ensuring improved resolution with a 110-nm-thick resist layer. This thickness is selected to match the smaller periodicity of the T-TM structures and facilitate the lift-off feasibility of the subsequent 50-nm-thick metal layer. Following the EBL step, the same metal deposition and lift-off processes as those employed for B-TE configurations are applied. Subsequently, the metal pattern, serving as a hard mask for the semiconductor grating, undergoes etching during the (Cl_2/N_2-based) ICP-RIE step at a rate of approximately $\sim$ 1.8 nm/s (i.e. mask-to-material etch selectivity of 0.37).

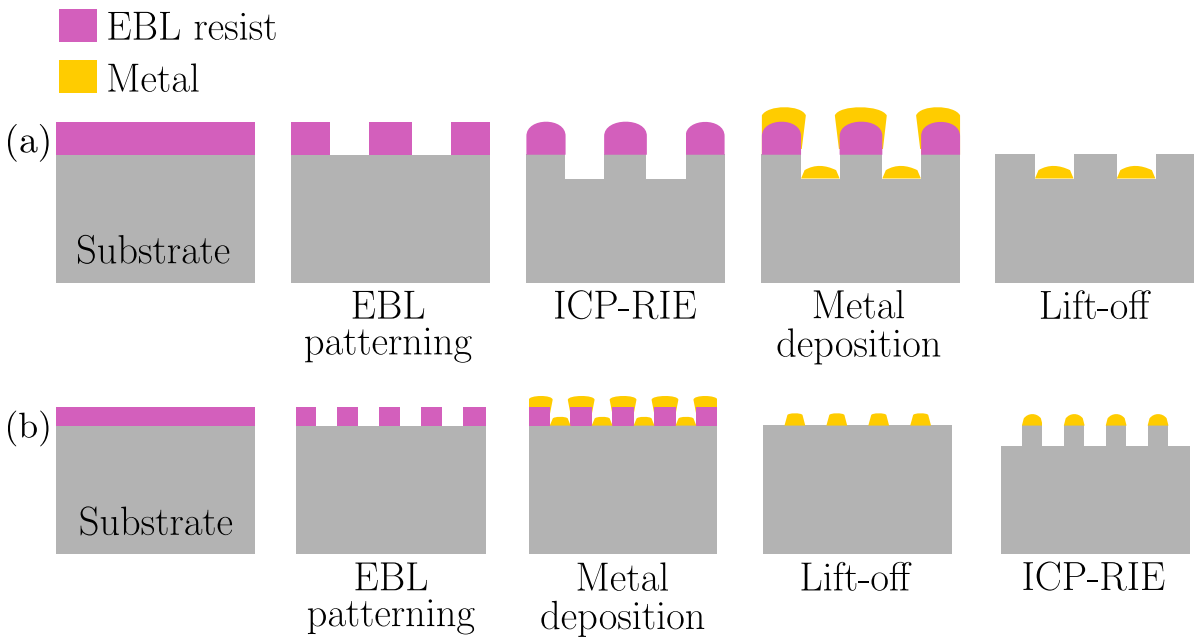

Figure S1: Fabrication process-flow of (a) B-TE configuration and (b) T-TM configuration.

In the B-TE process, the CSAR62 resist mask is effective in achieving relatively square and smooth etch profiles Figure 3). However, the initial undercut resist profile, formed during development, is eroded during the ICP-RIE etch, resulting in a humped profile. This humped profile contributes to undesired metal deposition on the upper part of the semiconductor-etched sidewall, leading to residual metal spots after lift-off along the grating lines. Their impact is somewhat mitigated by the accumulated metal on the resist sidewalls, which limits deposition on the GaAs flanks. This phenomenon explains why the B-TE structures could be fabricated using this process, resulting in the presence of metal residues at the top corners of the GaAs teeth after lift-off Figure 3).

Regarding the T-TM process, despite the increased difficulty of lifting off narrower lines (approximately 50 nm), the hard mask provided by metal stripes is advantageous as it allows self-alignment of GaAs and metal gratings. However, it comes with the drawback of rounding the metal stripes' profile, resulting in sloped etch walls (Figure 4).

Based on the structure designs summarized in table S1, seven structures have been fabricated using the processes described above. This table presents their measured dimensions and the associated uncertainties that are explained below.

Table S2: Summary of MetalMHCG measured parameters of the fabricated structures. The dimensions are extracted from the SEM images.

	MetalMHCG parameters				
Structure name	Λ (nm)	F	H (nm)	H_{Au} (nm)	H_{Ti} (nm)
B-TE-Au-1	170	0.49 ± 0.01	84 ± 5	40 ± 3	—
B-TE-Au-2a	210	0.53 ± 0.01	85 ± 5	36 ± 3	—
B-TE-Au-2b	210	0.39 ± 0.01	85 ± 5	36 ± 3	—
B-TE-TiAu-1	180	0.53 ± 0.01	89 ± 6	33 ± 5	5 ± 1
B-TE-TiAu-2	220	0.47 ± 0.01	107 ± 7	35 ± 4	5 ± 1
T-TM-Au	150	0.55 ± 0.01	29 ± 2[a] 31 ± 4[b]	56 ± 3[a] 49 ± 5[b]	—
T-TM-TiAu	100	0.57 ± 0.01	88 ± 6	27 ± 4	5 ± 1

[a] Clived cross-section.
[b] FIB-etched cross-section.

The fabricated MetalMHCG have dimension errors higher than 10% in most cases with respect to the targeted structures. Filling factors far from 0.5 were difficult to achieve by EBL. The GaAs height errors come from the process repeatability, as well as the aspect ratio dependent etching (ARDE) effect, which refers to the change of etch rates for features that have different aspect ratios. The highest differences between the targeted and fabricated dimensions is on the metal height. For the B-TE configuration fabrication, the deposition depends on the aspect ratio of the structure, and the deposition rate as a function of aspect ratio should be measured to reduce the error. In the T-TM configuration, the metal stripes act as a mask in the GaAs etching process. Since gold is slightly etched during plasma exposure, the deposited metal thickness must be adjusted to compensate this height reduction.

Fabrication for electrical sheet resistance characterization

Sets of 1, 2, 5, and 10 48-nm-thick gold nanowires were deposited on a GaAs NID substrate using EBL patterning and e-beam evaporation. The fabricated nanowires have lengths of 20 and 40 µm, a width of 60 nm, and a periodicity of 150 nm in sets of multiple nanowires. The extremities of each set were connected to TiAu contact pads for the two-probe measurement, as illustrated in Figure S2. Gold height was measured with atomic force microscopy, while W and L were measured using SEM, as shown in Figure S3.

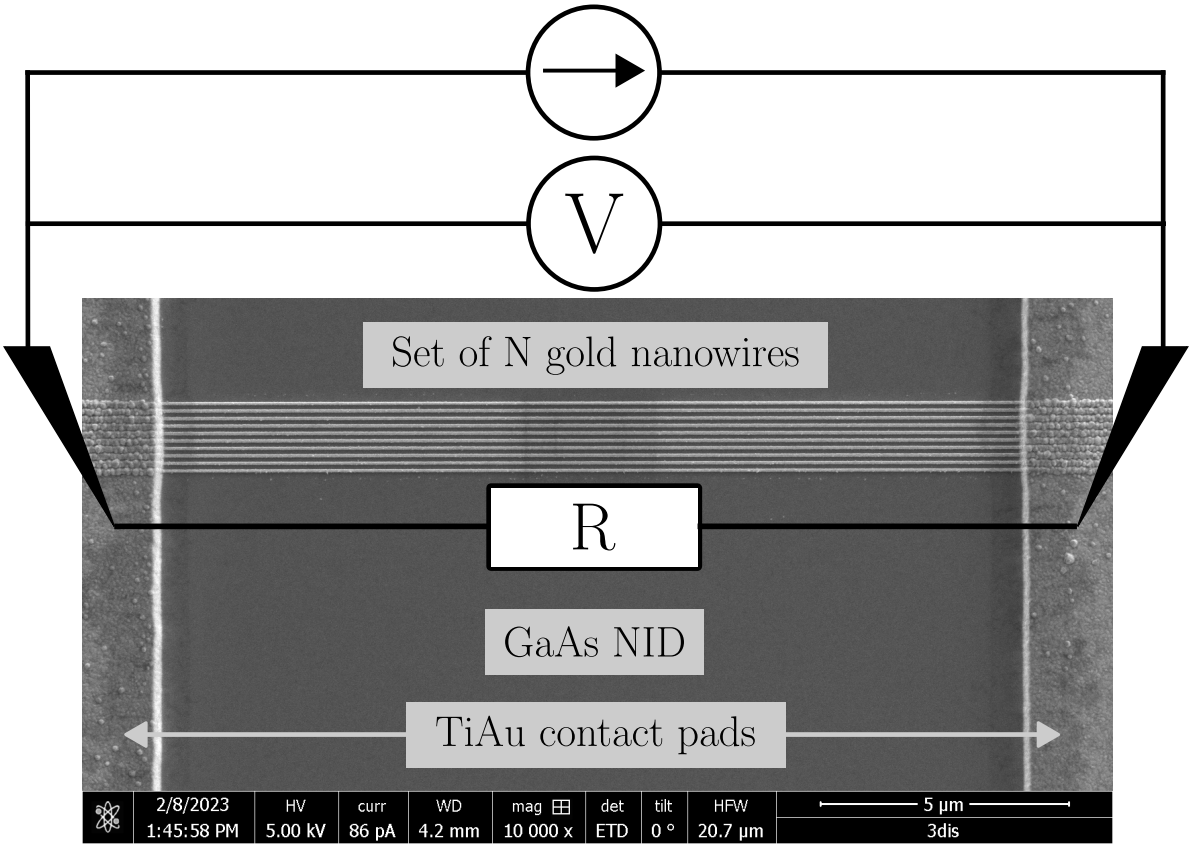

Figure S2: Schematic of the two-probes measurement principle of the resistance of a nanowire set.

3. Optical characterizations

3.1. Optical measurement setup

This setup is equipped with a Polarization Maintaining (PM) fibered tunable laser source (Broadsweeper BS-930-1-OEM), collimated with a variable zoom fiber collimator and a $\times 2$ beam expander (ZC618 and GBE02 from Thorlabs). The resulting beam is then focused on the sample using a 25 mm focal-length-lens, resulting in a Fourier-limited adjustable beam spot size. In the current experiments, the beam size was adjusted to $\sim$ 10µm, which is compatible with $40 \times 40\mu m^2$ fabricated pattern size. A half-wave plate allows polarization adjustment, and the transmitted light is collected through a $\times 20$ microscope objective equipped with an imaging lens and a camera, allowing precise alignment of the beam on the patterns. The reflected and transmitted signals are collected during these measurements with beam splitters and photodiodes. From these collected data, the transmission and reflection of the air/MetalMHCG/GaAs interface were extracted.

To mitigate Fabry-Pérot oscillations due to substrate thickness, a single-layer anti-reflective coating was applied on the substrate backside, although this was not perfectly optimized for the spectral range under study. Post-processing involved Fourier filtering

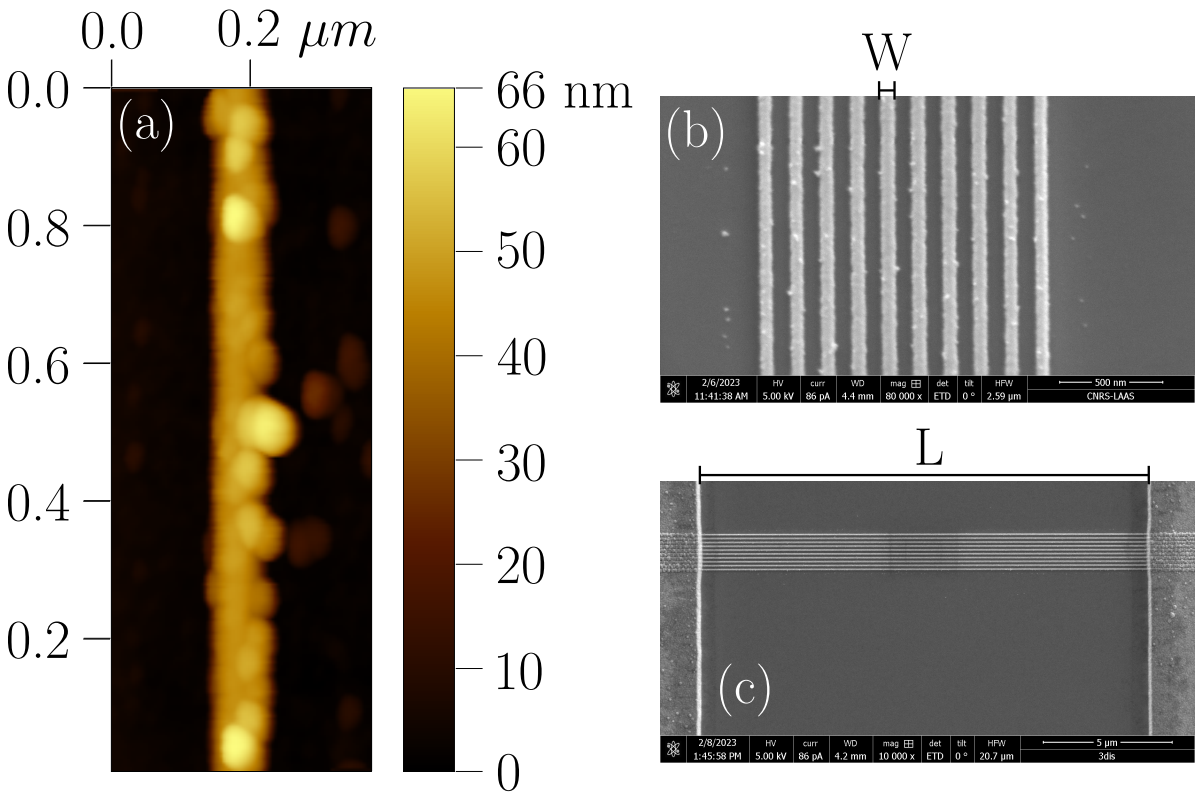

Figure S3: (a) Nanowire AFM height measurement, (b) SEM top-view image used for nanowire width measurement, and (c) SEM top-view image used for the measurement of the length between the contact pads.

to remove remaining tiny oscillations by keeping only the first 5% of the lowest harmonics of the signal in the Fourier space.

Optical properties of fabricated MetalMHCG structures

The transmission and reflection coefficients measured at normal incidence in the 900-985 nm spectral range are presented in Figures S4 and S5, and main results for each fabricated structures are summarized in Table S3.

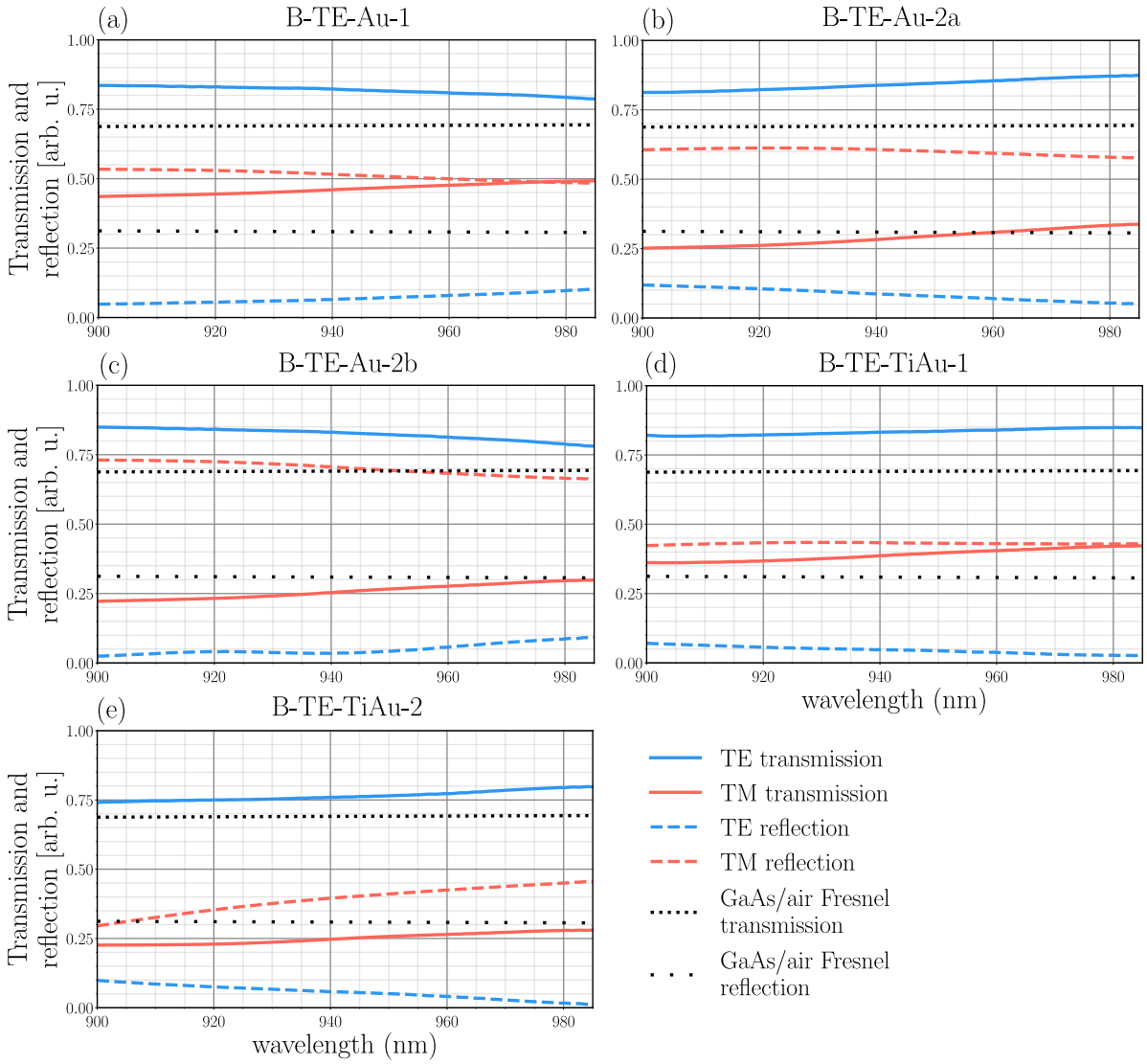

Figure S4: Spectroscopy measurements of fabricated B-TE configurations at normal incidence between 900 and 985 nm.

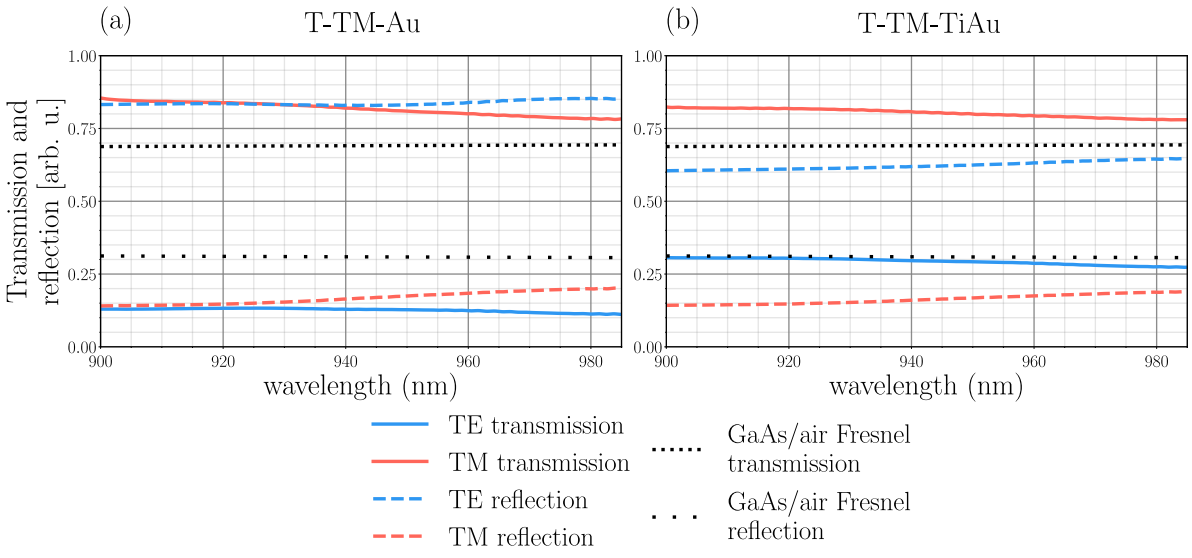

Figure S5: Spectroscopy measurements of fabricated T-TM configurations at normal incidence between 900 and 985 nm.

Table S3: Summary of transmission (T), reflection (R), and Losses $= 1 - R - T$ from measurements in Figures S4 and S5.

Structure name	T (940 nm)		R (940 nm)		Losses (940 nm)[a]	
	TE	TM	TE	TM	TE	TM
B-TE-Au-1	**0.82**	0.46	0.06	0.51	0.12	0.03
B-TE-Au-2a	**0.84**	0.28	0.09	0.61	0.07	0.11
B-TE-Au-2b	**0.83**	0.25	0.03	0.70	0.14	0.05
B-TE-TiAu-1	**0.83**	0.38	0.05	0.43	0.12	0.19
B-TE-TiAu-2	**0.76**	0.25	0.06	0.39	0.18	0.36
T-TM-Au	0.13	**0.82**	0.83	0.16	0.04	0.02
T-TM-TiAu	0.29	**0.81**	0.62	0.16	0.09	0.03

[a] Absorption and light scattering.

4. Optical simulations based on measured dimensions and profiles

Post-fabrication numerical simulations of the optical properties of the MetalMHCG structures, incorporating uncertainties in dimensions based on the grating's geometrical parameters and the measured profile from SEM images, have been performed.

The numerical simulations are based on the Plane Wave Admittance Method (PWAM) as proposed in [1], which offers a solution to fully vectorial Maxwell's equations and has been demonstrated to be in a good agreement with experimental findings [2, 3]. In our analyses, we consider the grating to be infinite along the x-direction and enforce periodic boundary conditions at the boundaries of a single grating stripe. To ensure an accurate representation of the experimental geometry, we employ 60 plane waves to minimize numerical errors. Both of the polarizations are investigated in our study: in the transverse electric field (TE) configuration, the electric field aligns parallel to the stripes, whereas in the transverse magnetic configuration (TM), it is perpendicular to them (See Fig. S6).

Utilizing numerical software, we were able to accurately map the real shape of the grating for each configuration based on SEM image. We outlined the shape of the grating, and then, employing the least square method, we transferred the design into a form of rectangles, as illustrated in Fig. S7. This approach facilitated more detailed simulations and enabled us to align more closely with experimental results. In the case of the experimental shape, we took into account parameters such as the height of the grating slab and gold, as well as the width of the slab.

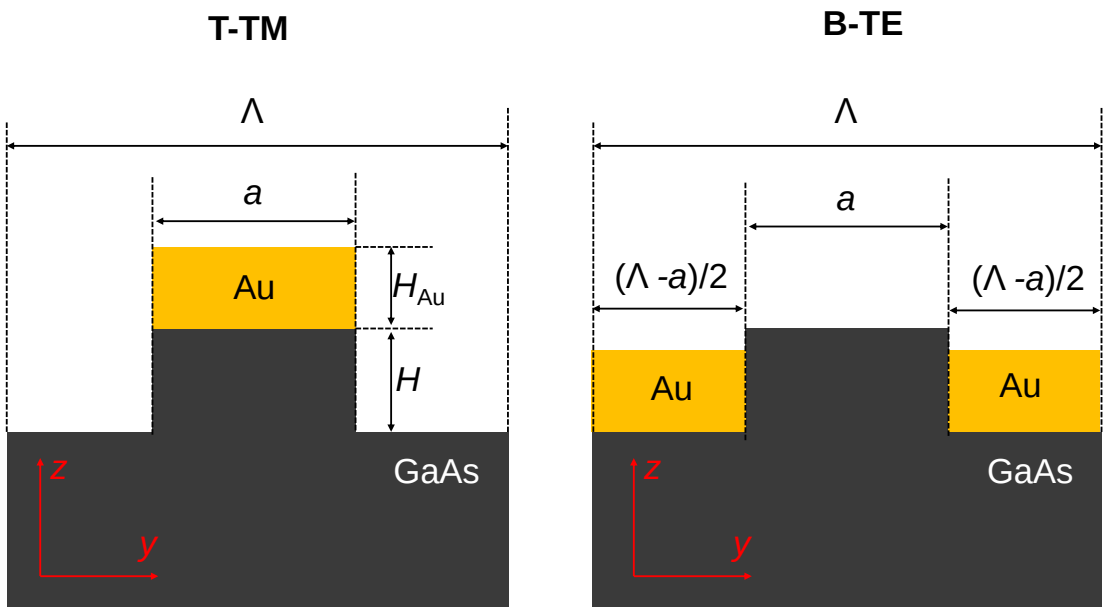

Figure S6: Geometrical designs with construction parameters taken into account in the simulations for two polarizations (T-TM - left panel, B-TE - right panel). H and H_{Au} are the height of the grating slab and metal respectively, a is the width of a single slab, Λ period of a grating. Additionally fill factor F is considered and defined as $F = a/\Lambda$.

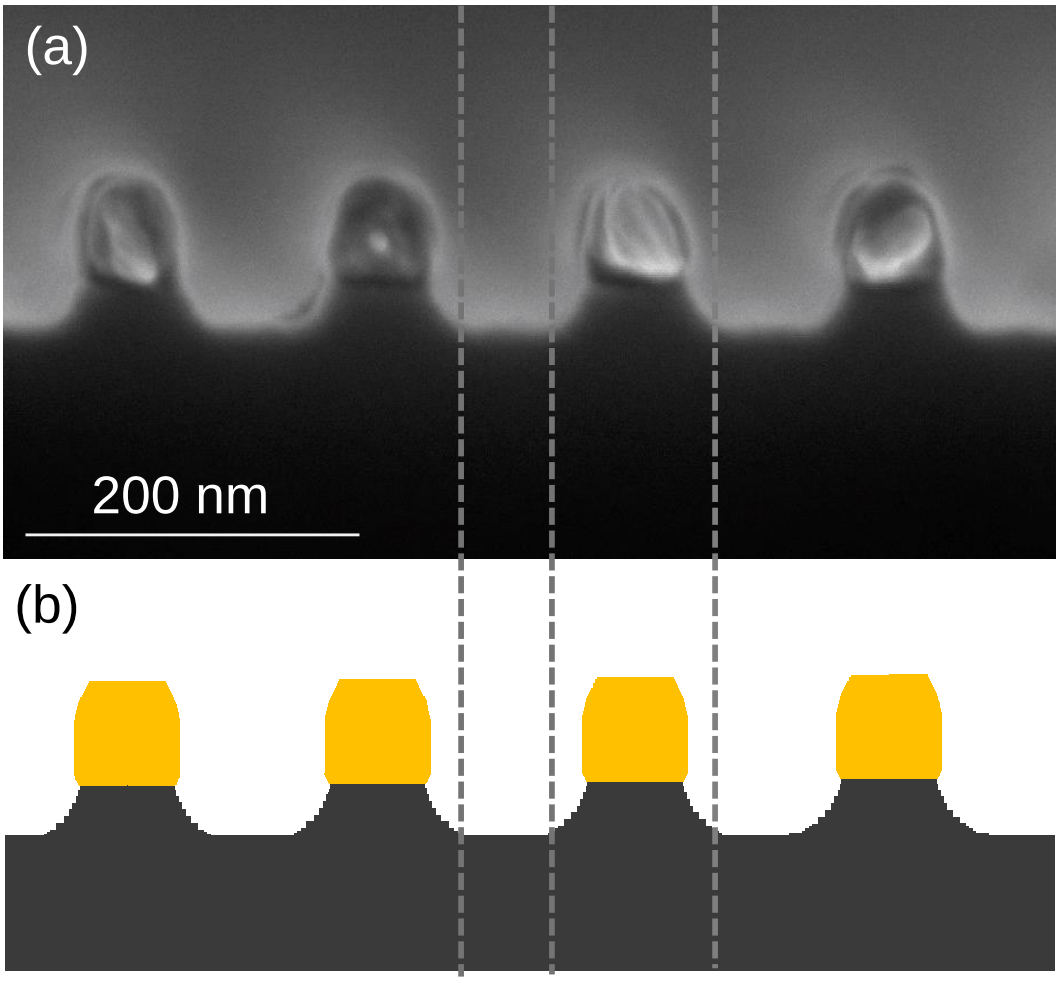

Figure S7: (a) SEM image of a real structure for T-TM configuration. (b) Geometrical representation of T-TM configuration used in simulations.

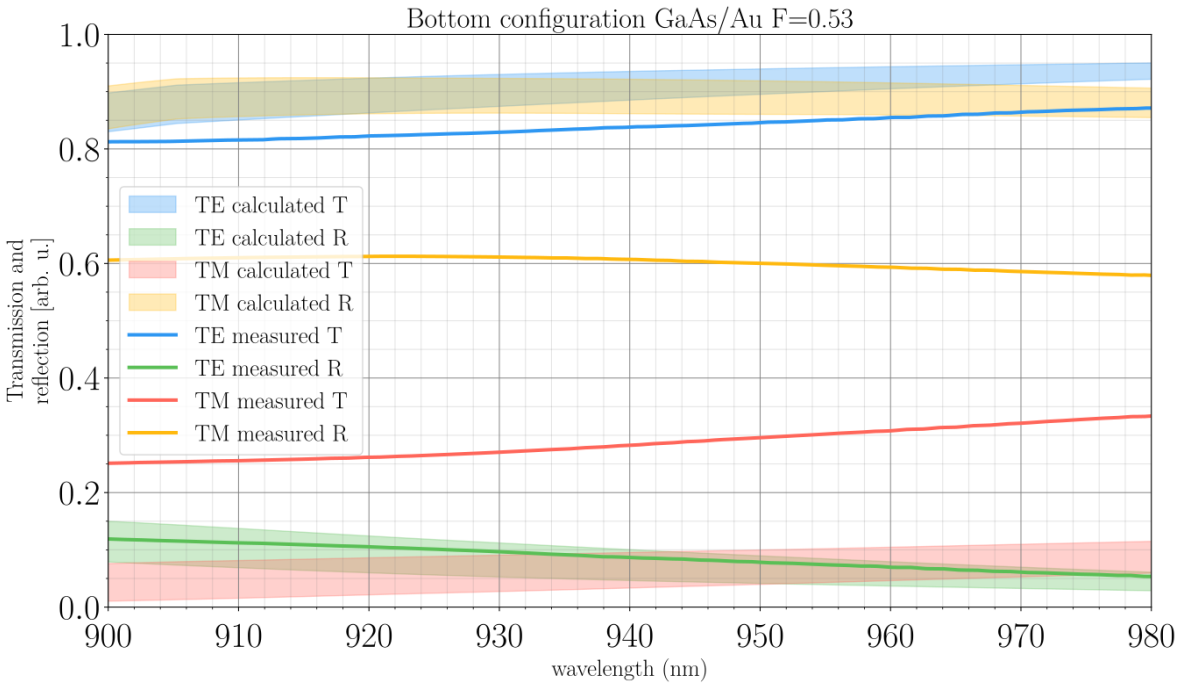

Figure S8: Optical transmission and reflectivity in both polarizations of the B-TE-Au-2a sample (F=0.53): solid lines represent the measured curves, while corresponding post-fabrication simulations are depicted as bands, representing the uncertainties in the geometric parameters measured.

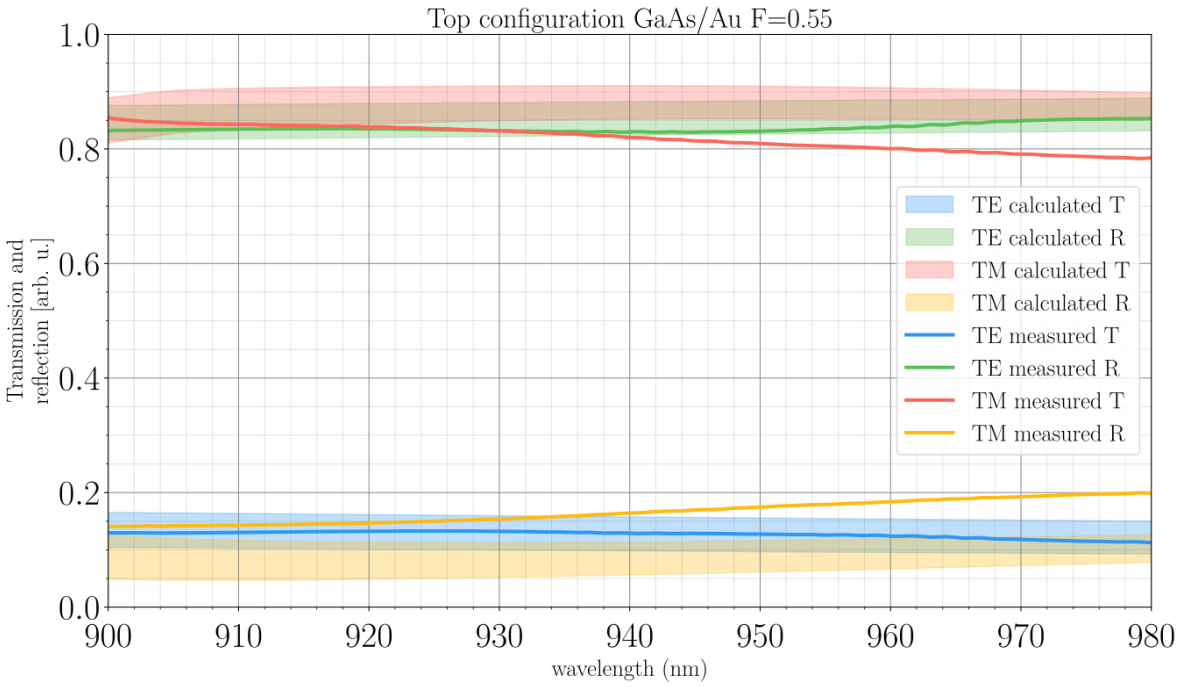

Figure S9: Optical transmission and reflectivity in both polarizations of the T-TM-Au sample (F=0.55): solid lines represent the measured curves, while corresponding post-fabrication simulations are depicted as bands, representing the uncertainties in the geometric parameters measured.

5. Impact of corrugated grating sidewalls

The real-world corrugation of the sidewalls of MetalMHCG structures is modeled based on the approach demonstrated in [4], which closely aligns with three-dimensional reflectance calculations of MHCGs, as analyzed in [5]. In our model, each stripe width is scaled by a factor ranging from 0 to 1, sampled from a normal distribution. For a given standard deviation, five values are drawn from this distribution to construct an MetalMHCG with periodic boundary conditions, where each set of 5 stripes features unique width variations. The optical power transmittance spectrum at normal incidence is then calculated for each grating. This sampling process, generating a random set of stripe widths, is repeated 100 times to produce 100 unique gratings. For each of these 100 MetalMHCG structures, the arithmetic mean of the optical power transmittance spectrum is computed. This averaged spectrum represents the final simulated result shown in Fig. S10, which is displayed for standard deviations ranging from 0.02 to 0.1. Based on SEM images of processed MetalMHCG structures, the standard deviation of sidewall corrugation is estimated at 0.046.

6. Optical power transmittance *vs* sheet resistance

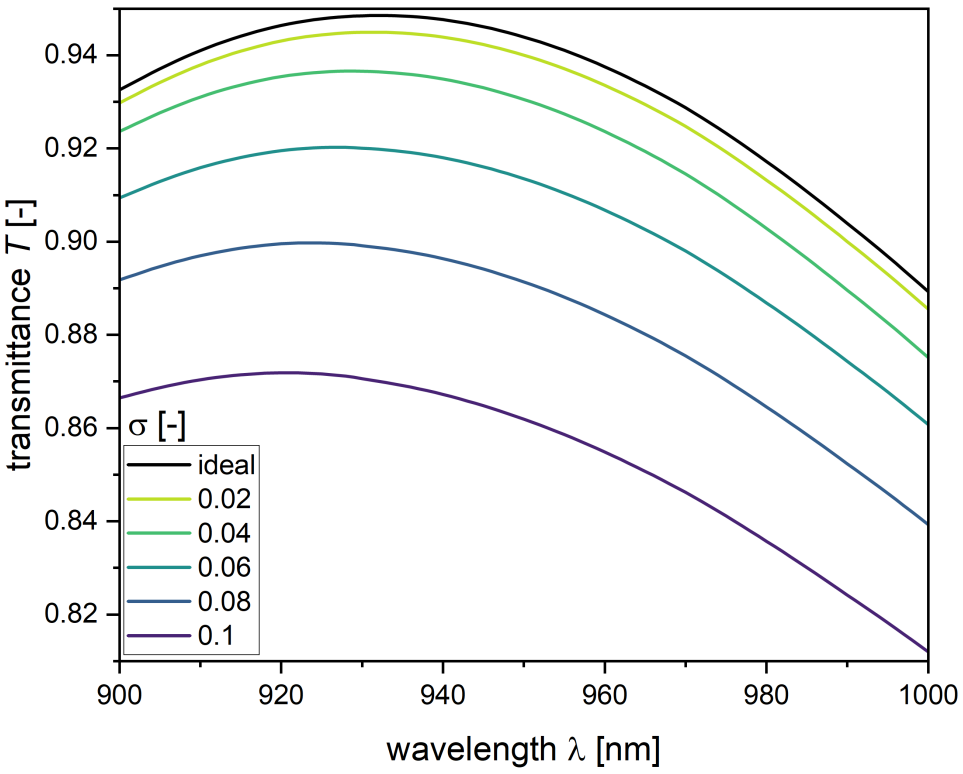

Figure S10: Optical power transmittance spectra for B-TE-Au-1 defined in main text for different level of grating aperiodicity determined by standard deviation in normal distribution.

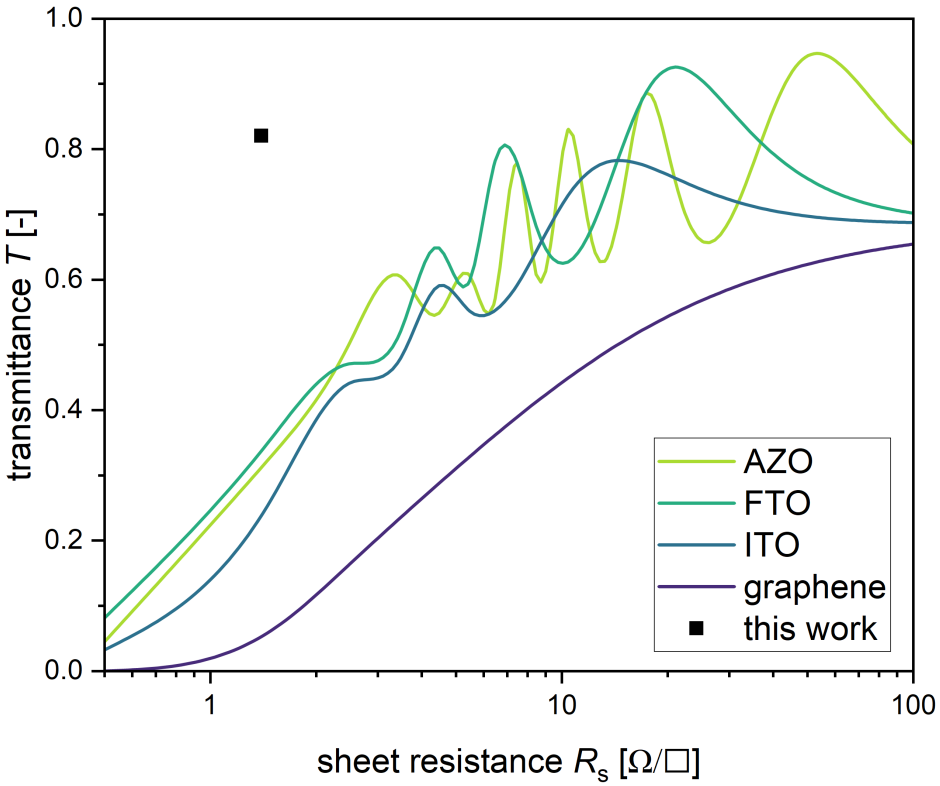

Figure S11: Calculated optical power transmittance at 940 nm through GaAs interface covered woth different TCEs as the function of sheet resistance of AZO, FTO, ITO and graphene. Their optical and electrical properties were assumed based on references presented in Table S1. Black dots represent MetalMHCGs measured for polarised light.

Table S4: Refractive indices of TCE.

	n @ 940 nm	k @ 940 nm	Reference
ITO	1.3316	0.054116	[6] (Numerical data kindly provided by Manuela Schiek)
FTO	2.05	0.0378	[7]
AZO	1.6183	0.014	[8]
Graphene	3.02	1.8969	[9]

Table S5: Refractive indices of TCE.

Material	Resistivity ($\Omega.cm$)	Reference
ITO	2.20×10^{-4}	[10]
FTO	2.31×10^{-4}	[11]
AZO	7.60×10^{-4}	[12]
Graphene	1.05×10^{-5}	[13]

References

[1] M. Dems, R. Kotynski, and K. Panajotov, "Plane wave admittance method - a novel approach for determining the electromagnetic modes in photonic structures," *Optics Express*, vol. 13, no. 9, p. 3196, 2005.

[2] E. Pruszyńska-Karbownik, D. Jandura, M. Dems, Ł. Zinkiewicz, A. Broda, M. Gębski, J. Muszalski, D. Pudiš, J. Suffczyński, and T. Czyszanowski, "Concept of inverted refractive-index-contrast grating mirror and exemplary fabrication by 3d laser micro-printing," *Nanophotonics*, vol. 12, no. 18, pp. 3579–3588, Aug. 2023.

[3] M. Ekielski, W. G, K. Bogdanowicz, M. Ryga, M. Mikulicz, P. Śpiewak, M. Kowalski, M. Gebski, M. Motyka, A. Szerling, and T. Czyszanowski, "Monolithic high contrast grating integrated with metal: Infrared electrode with exceptionally high conductivity and transmission," *Advanced Functional Materials*, vol. n/a, no. n/a, p. 2312392, Dec. 2023. [Online]. Available: https://onlinelibrary.wiley.com/doi/abs/10.1002/adfm.202312392

[4] M. Marciniak, A. Broda, M. Gębski, M. Dems, J. Muszalski, A. Czerwinski, J. Ratajczak, L. Marona, W. Nakwaski, J. A. Lott, and T. Czyszanowski, "Tuning of reflection spectrum of a monolithic high-contrast grating by variation of its spatial dimensions," *Optics Express*, vol. 28, no. 14, p. 20967, Jun. 2020.

[5] M. Marciniak, T.-S. Chang, T.-C. Lu, F. Hjort, Haglund, L. Marona, M. Gramala, P. Modrzyński, R. Kudrawiec, K. Sawicki, R. Bożek, W. Pacuski, J. Suffczyński, M. Gbski, A. Broda, J. Muszalski, J. A. Lott, and T. Czyszanowski, "Impact of stripe shape on the reflectivity of monolithic high contrast gratings," *ACS Photonics*, vol. 8, no. 11, pp. 3173–3184, Oct. 2021.

[6] A. Minenkov, S. Hollweger, J. Duchoslav, O. Erdene-Ochir, M. Weise, E. Ermilova, A. Hertwig, and M. Schiek, "Monitoring the electrochemical failure of indium tin oxide electrodes via operando ellipsometry complemented by electron microscopy and spectroscopy," *ACS Applied Materials & Interfaces*, vol. 16, no. 7, pp. 9517–9531, Feb. 2024.

[7] S. B. Ameur, A. Barhoumi, H. Bel hadjltaief, R. Mimouni, B. Duponchel, G. Leroy, M. Amlouk, and H. Guermazi, "Physical investigations on undoped and fluorine doped sno2 nanofilms on

flexible substrate along with wettability and photocatalytic activity tests," *Materials Science in Semiconductor Processing*, vol. 61, pp. 17–26, Apr. 2017.

[8] R. E. Treharne, A. Seymour-Pierce, K. Durose, K. Hutchings, S. Roncallo, and D. Lane, "Optical design and fabrication of fully sputtered cdte/cds solar cells," *Journal of Physics: Conference Series*, vol. 286, p. 012038, Mar. 2011.

[9] M. A. El-Sayed, G. A. Ermolaev, K. V. Voronin, R. I. Romanov, G. I. Tselikov, D. I. Yakubovsky, N. V. Doroshina, A. B. Nemtsov, V. R. Solovey, A. A. Voronov, S. M. Novikov, A. A. Vyshnevyy, A. M. Markeev, A. V. Arsenin, and V. S. Volkov, "Optical constants of chemical vapor deposited graphene for photonic applications," *Nanomaterials*, vol. 11, no. 5, p. 1230, May 2021.

[10] B.-R. Koo, D.-H. Oh, D.-H. Riu, and H.-J. Ahn, "Improvement of transparent conducting performance on oxygen-activated fluorine-doped tin oxide electrodes formed by horizontal ultrasonic spray pyrolysis deposition," *ACS Applied Materials & Interfaces*, vol. 9, no. 51, pp. 44 584–44 592, Dec. 2017.

[11] H.-l. SHEN, H. ZHANG, L.-f. LU, F. JIANG, and C. YANG, "Preparation and properties of azo thin films on different substrates," *Progress in Natural Science: Materials International*, vol. 20, pp. 44–48, Nov. 2010.

[12] R. A. Maniyara, C. Graham, B. Paulillo, Y. Bi, Y. Chen, G. Herranz, D. E. Baker, P. Mazumder, G. Konstantatos, and V. Pruneri, "Highly transparent and conductive ito substrates for near infrared applications," *APL Materials*, vol. 9, no. 2, Feb. 2021.

[13] R. Murali, K. Brenner, Y. Yang, T. Beck, and J. D. Meindl, "Resistivity of graphene nanoribbon interconnects," *IEEE Electron Device Letters*, vol. 30, no. 6, pp. 611–613, Jun. 2009.